

## Hyperspectral aerosol optical depths from TCAP flights

Y. Shinozuka,<sup>1,2</sup> R. R. Johnson,<sup>3</sup> C. J. Flynn,<sup>4</sup> P. B. Russell,<sup>3</sup> B. Schmid,<sup>4</sup> J. Redemann,<sup>3</sup> S. E. Dunagan,<sup>3</sup> C. D. Kluzek,<sup>4</sup> J. M. Hubbe,<sup>4</sup> M. Segal-Rosenheimer,<sup>3</sup> J. M. Livingston,<sup>5</sup> T. F. Eck,<sup>6,7</sup> R. Wagener,<sup>8</sup> L. Gregory,<sup>8</sup> D. Chand,<sup>4</sup> L. K. Berg,<sup>4</sup> R. R. Rogers,<sup>9</sup> R. A. Ferrare,<sup>9</sup> J. W. Hair,<sup>9</sup> C. A. Hostetler,<sup>9</sup> and S. P. Burton<sup>9</sup>

Received 19 July 2013; revised 4 October 2013; accepted 22 October 2013.

[1] The 4STAR (Spectrometer for Sky-Scanning, Sun-Tracking Atmospheric Research), a hyperspectral airborne Sun photometer, acquired aerosol optical depths (AOD) at 1 Hz during all July 2012 flights of the Two-Column Aerosol Project. Root-mean-square differences from Aerosol Robotic Network ground-based observations were 0.01 at wavelengths between 500–1020 nm, 0.02 at 380 and 1640 nm, and 0.03 at 440 nm in four clear-sky fly-over events, and similar in ground side-by-side comparisons. Changes in the above-aircraft AOD across 3 km deep spirals were typically consistent with integrals of coincident in situ (on Department of Energy Gulfstream 1 with 4STAR) and lidar (on NASA B200) extinction measurements within 0.01, 0.03, 0.01, 0.02, 0.02, and 0.02 at 355, 450, 532, 550, 700, and 1064 nm, respectively, despite atmospheric variations and combined measurement uncertainties. Finer vertical differentials of the 4STAR measurements matched the in situ ambient extinction profile within 14% for one homogeneous column. For the AOD observed between 350 and 1660 nm, excluding strong water vapor and oxygen absorption bands, estimated uncertainties were  $\sim 0.01$  and dominated by (then) unpredictable throughput changes, up to  $\pm 0.8\%$ , of the fiber optic rotary joint. The favorable intercomparisons herald 4STAR's spatially resolved high-frequency hyperspectral products as a reliable tool for climate studies and satellite validation.

**Citation:** Shinozuka, Y., et al. (2013), Hyperspectral aerosol optical depths from TCAP flights, *J. Geophys. Res. Atmos.*, 118, doi:10.1002/2013JD020596.

### 1. Introduction

[2] Since 1985, the NASA Ames airborne tracking Sun photometers (AATS-6 and AATS-14) [Russell et al., 1986; Matsumoto et al., 1987] have made extensive measurements of atmospheric constituents via their effect on the Sun's direct beam transmission through the atmosphere. Constituents measured to date include aerosols (see, for example, Livingston et al. [2003], Schmid et al. [2003b], Russell et al. [2007], Redemann et al. [2009], and Shinozuka et al. [2011]), ozone [Livingston et al., 2005; Swartz et al., 2005; Pitts et al., 2006] and water vapor [Ferrare et al., 2000; Livingston et al., 2000; Pilewskie et al., 2000; Schmid et al., 2000, 2001;

Livingston et al., 2003; Redemann et al., 2003; Revercomb et al., 2003; Schmid et al., 2003a; Ferrare et al., 2006; Livingston et al., 2007, 2008]. AATS measurements are used extensively to validate and supplement satellite retrievals of stratospheric and tropospheric constituents, validate airborne and ground-based lidar data products, characterize horizontal and vertical distributions of gas and aerosol properties, study closure (consistency) with in situ samplers aboard many aircraft, test chemical-transport models, and study the radiative effects of atmospheric constituents and earth surfaces that are important to both climate and remote measurements. AATS measurements and analyses have been described in more than 100 publications since 1987. Other airborne Sun photometers have been deployed elsewhere [Asseng et al., 2004; Zieger et al., 2007; Karol et al., 2013].

[3] As satellite capabilities continue to improve, so too must the capabilities of airborne instruments, enabling satellite and aircraft measurements to advance together in answering the increasingly difficult questions about the extent of Earth's climate variability and its likely causes. The need to provide greatly expanded measurement capabilities led to the concept of the Spectrometer for Sky-Scanning, Sun-Tracking Atmospheric Research (4STAR). The 4STAR combines the proven airborne Sun-tracking ability of the current AATS-14 with the sky-scanning ability of the ground-based Aerosol Robotic Network (AERONET) Sun/sky photometers, while, for the

<sup>1</sup>NASA ARC-CREST, Moffett Field, California, USA.

<sup>2</sup>Bay Area Environmental Research Institute, Sonoma, California, USA.

<sup>3</sup>NASA Ames Research Center, Moffett Field, California, USA.

<sup>4</sup>Pacific Northwest National Laboratory, Richland, Washington, USA.

<sup>5</sup>SRI International, Menlo Park, California, USA.

<sup>6</sup>Universities Space Research Association, Columbia, Maryland, USA.

<sup>7</sup>NASA Goddard Space Flight Center, Greenbelt, Maryland, USA.

<sup>8</sup>Brookhaven National Laboratory, Upton, New York, USA.

<sup>9</sup>NASA Langley Research Center, Hampton, Virginia, USA.

Corresponding author: Y. Shinozuka, Bay Area Environmental Research Institute, 596 1st St W, Sonoma, CA 95476, USA.  
(Yohei.Shinozuka@nasa.gov)

©2013. American Geophysical Union. All Rights Reserved.  
2169-897X/13/10.1002/2013JD020596

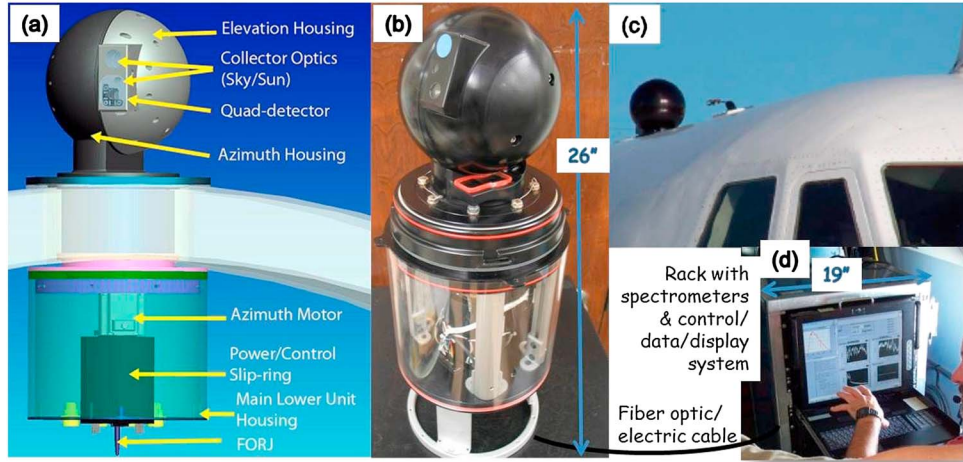


**Figure 1.** (a) Design for 4STAR tracking/scanning head and can. (b) Head and can as built. (c) The 4STAR head on G-1 aircraft. (d) Rack and contents flying on G-1.

first time to our knowledge, extending these capabilities by providing full spectral information from the ultraviolet to the shortwave infrared (SWIR). The instrument is in a compact, rugged, airworthy package capable of delivering information about atmospheric constituents and their effects on radiant energy while operating in the difficult environment extending both outside and inside the aircraft cabin (Figure 1).

[4] The 4STAR flew its first science mission, the U.S. Department of Energy (DOE) Two-Column Aerosol Project (TCAP) Phase 1, in July 2012. The DOE Atmospheric Radiation Measurement (ARM) Aerial Facility Gulfstream 1 (G-1) flight paths out of the Barnstable Municipal Airport, Hyannis, Massachusetts, are shown in Figure 2, together with the DOE ARM Mobile Facility ground station at the Highlands Center on Cape Cod. Among the objectives of this multiplatform experiment is evaluation of model simulations for aging anthropogenic aerosols. The 4STAR measurements of aerosol optical depth (AOD) and its wavelength dependence along the air mass transport paths from the U.S. East Coast to the Atlantic Ocean provide valuable information to accomplish this objective.

[5] The 4STAR operated successfully during every single flight and on the ground. It exercised every designed operational mode, collecting airborne data in Sun-tracking, sky-scanning, and zenith-viewing modes. This paper reports on the measured AOD spectra, with focus on comparisons to coincident measurements by other suborbital instruments. Separate papers discuss 4STAR's other science products such as column contents of water vapor, ozone, and nitrogen dioxide [Segal-Rosenheimer *et al.*, 2013b]. Dunagan *et al.* [2013] detail the design, functions, and uncertainties related to all modes of operation.

## 2. Instrumentation

### 2.1. The 4STAR

[6] The 4STAR comprises a movable optical head that extends through the top of the aircraft fuselage, an instrument rack housed within the aircraft, and umbilical connections between the two. The 4STAR optical head incorporates two distinct sets of optics with different throughput and field of

view (FOV)—a sunlight collector for use when tracking the Sun and a skylight collector for sky radiance measurements. A three-position mechanical shutter permits selection of either collector or a closed-opaque position. Azimuth and elevation motors in the head permit orientation of the optical collectors (fixed with respect to each other) to any point above the hemisphere in the aircraft frame.

[7] While Sun tracking, active alignment to the solar disk relies on the differential analog signal provided by a quadrant photodiode detector coaligned with the Sun collector. During the July phase of TCAP, the tracking error was generally  $<0.1^\circ$  on horizontal flight legs and  $<0.2^\circ$  during vertical spirals, well within specifications designed to keep the Sun within the instrument's sunlight collector FOV. The tracking error seldom exceeded  $0.7^\circ$ , beyond which point the system's response decreases by  $>1\%$  as determined by FOV measurements, methodical scan across the solar disk.

[8] The 4STAR incorporates several new technologies compared to its filter-based AATS-6 and AATS-14 predecessors. The electrical cables in the umbilical provide power to the head and carry electrical signals for motion control and monitoring back to the instrument rack. The optical signal is carried from the head through a fiber optic rotary joint (FORJ) and custom fiber optic waveguides to two fiber-coupled spectrometers housed in the instrument rack. The spectrometers are integrated packages, each incorporating a diffracting grating, a detector array, and detection electronics.

[9] For TCAP, the two spectrometers were as follows:

[10] 1. ultraviolet-visible-near-infrared (UV-VIS-NIR), 210–995 nm: Tec5 multichannel spectrometer with a 1044-channel Hamamatsu S7031-1006 charge-coupled device detector, full width at half maximum (FWHM) 2–3 nm up to 850 nm and 3–7 nm above, and spectral sampling interval 0.8 nm across the wavelengths.

[11] 2. SWIR, 950–1703 nm: Tec5 near infrared plane grating spectrometer 1.7 with a 512-channel Sensors Unlimited (SU) Inc. Multiplexed Indium Gallium Arsenide (InGaAs) SU 512LD-1.7 T1 diode array, FWHM  $\sim 5$  nm, sampling interval  $\sim 1.5$  nm.

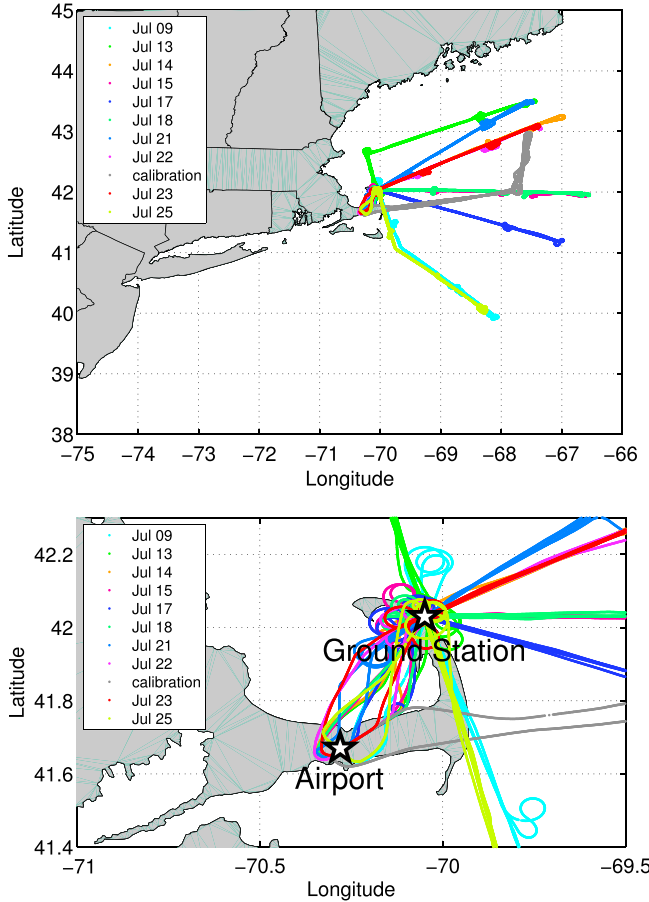


**Figure 2.** The flight track of G-1 aircraft during TCAP Phase 1. Also marked are the Barnstable Airport, Hyannis, Massachusetts, and the ground station. Some flights took largely overlapping paths. All science flights except the second one on 22 July 2012 (see Appendix A, grey curve) flew a two-column altitude pattern exemplified in Figure 3, the first column over the ocean and the second over the ground station.

[12] Both spectrometers and accompanying read out electronics are temperature stabilized. The sampling rate was 1 Hz. The analog-to-digital converted counts were stored together with data on instrument tracking, temperature control, aircraft location and position, ambient temperature, relative humidity (RH), static pressure, and other relevant information. Dark counts were measured once in 20 min with the shutter covering both collectors.

[13] AOD data acquisition, screening, reduction, calibration, and uncertainty analysis follow a similar approach to AATS-6 and AATS-14 [Matsumoto et al., 1987; Russell et al., 1993a, 1993b; Schmid and Wehrli, 1995; Schmid et al., 1996, 1998; Russell et al., 1999; Schmid et al., 2001; Livingston et al., 2003; Redemann et al., 2003; Schmid et al., 2003a; Livingston et al., 2005; Redemann et al., 2005; Livingston et al., 2007; Russell et al., 2007; Livingston et al., 2009; Redemann et al., 2009; Shinozuka et al., 2011].

[14] We first calculate count rate,  $C$ , by subtracting the dark counts from the raw counts and dividing the result by the integration time. The integration time was set at 50 ms for the UV-VIS-NIR detector and 400 ms for the SWIR during

TCAP. We averaged six 50 ms measurements of the UV-VIS-NIR spectrometer. We did not average the SWIR measurements. The detectors were left idle for the remainder of the time (read out time). Instability in the dark counts contributed an uncertainty well below 0.001 optical depth in absolute terms for the UV-VIS-NIR. The contribution is near 0.001 for all SWIR aerosol channels except above 1500 nm where it is closer to 0.003.

[15] We apply two tests to screen the measurements for interference by clouds following the approach of Schmid et al. [2003a] and Redemann et al. [2009]. The first uses the standard deviation of the count rate to examine the spatiotemporal variability of the transmission measurements, and the second uses the Angstrom exponent derived from the calculated AOD. In particular, for the TCAP July data, the standard deviation of the count rate was calculated over 9 s (or  $\sim 1$  km during horizontal legs) running intervals at 501 and 1236 nm, and data points with a standard deviation that exceeded an arbitrary, predetermined threshold were classified as cloudy. Separately, the variability of the Angstrom exponent is used to decide whether a feature that shows large spatial variability is likely a cloud or an aerosol plume. If, for example, a feature shows large transmission variability and a decrease in Angstrom exponent, we conclude that the feature is likely a cloud and flag it accordingly. If, on the other hand, a feature shows large transmission variability but no change in Angstrom exponent when compared to adjacent measurements, we conclude that the feature is an aerosol plume. We concede that our method may contain remnants of cirrus cloud contamination if the optical depth of such cirrus clouds is small enough so as to not significantly affect the Angstrom exponent calculations of the combined aerosol-cirrus optical depth. We estimate such cirrus contaminations to be possible at levels of 10–20% of AOD, generally equivalent to optical depths of 0.01–0.02 or less. We are building a more robust automatic cirrus filtering method based on our previous research [Segal-Rosenheimer et al., 2013a]. Another potentially large source of error is dirt deposited on the Sun photometer entrance window [Livingston et al., 2003]. To minimize this error we cleaned the window carefully before each flight. Frost, condensation, dirt, and adhesive particles would be indicated by abrupt changes in transmission and resulting small transmissions (large derived AOD) during high-altitude legs. None of the July 2012 TCAP flights is obviously affected by them, except for the first leg of the first transit flight that is not presented in this paper.

[16] For the wavelengths ( $\lambda$ ) unaffected by strong water vapor or oxygen absorption, we retrieve AOD from the slant path transmissions using the methodology built on the Beer-Lambert law and described in detail previously [Russell et al., 1993a].

$$\tau_p(\lambda) = (\ln C_0'(\lambda) - \ln C(\lambda) - m_R \tau_R(\lambda) - \Sigma m_g \tau_g(\lambda)) / m_p \quad (1)$$

where

$$C_0'(\lambda) = (R_m/R)^2 C_0(\lambda) \quad (2)$$

and  $C_0$  is the count rate that would be measured at the top of the atmosphere at the mean Sun-Earth distance  $R_m$ .  $R$  is the distance during the measurements.  $m$  is the air mass factor, computed separately for Rayleigh scattering (denoted  $R$ ),

gas components (ozone, nitrogen dioxide, etc., collectively denoted  $g$ ), and particles ( $p$ ). We estimate the relative uncertainty in the calculated air mass factors to be 1% at most.

[17] We reduce equation (1) to

$$\tau_p(\lambda) = (\ln C_0'(\lambda) - \ln C_p(\lambda)) / m_p \quad (3)$$

by augmenting the count rate for the Rayleigh scattering and gas absorption

$$C_p(\lambda) = C(\lambda) \exp(m_R \tau_R(\lambda) + \sum m_g \tau_g(\lambda)) \quad (4)$$

[18] The atmospheric molecular scattering  $\tau_R$  was calculated after *Bucholtz* [1995]. A 1.5% relative uncertainty was assumed for the parameterization and atmospheric pressure measurement combined. The absorption by weakly absorbing gas species was computed as the product of each species' density and cross section. For this study, ozone ( $O_3$ ) column contents were extracted from the Ozone Monitoring Instrument (OMI) L2 archived retrieval files and adjusted for the G-1 altitude using the 1976 standard ozone model vertical distribution, similar to some of the previous AATS studies [*Schmid et al.*, 2006; *Livingston et al.*, 2007, 2009]. A relative uncertainty of 5% was assumed. Nitrogen dioxide ( $NO_2$ ) column density was also obtained from OMI L2 products, with an assumed uncertainty of 27%. Oxygen dimer ( $O_2-O_2$ ) column density was computed for the aircraft altitude, with an assumed uncertainty of 12%.  $O_3$  and  $NO_2$  high spectral resolution cross sections were calculated using the Bogumil temperature-dependent ozone cross-section database [*Bogumil et al.*, 2003] at 243 K and *Vandaele et al.* [1998], respectively. Both were convolved with the spectrometer near symmetric Gaussian point spread function, which has a wavelength-dependent FWHM resolution of 2–3 nm in the spectral ranges where these gases strongly absorb.  $O_2-O_2$  cross sections were taken from the new Collision Induced Absorption Database in HITRAN [*Richard et al.*, 2012]. For this paper, water vapor and oxygen were not separated from aerosols within each wavelength. Instead, we focus our attention on the wavelengths affected minimally by these strong absorbers.

[19] Through its nonzero FOV, the 4STAR detector receives some diffuse light that has undergone one or more scattering events, in addition to the direct solar beam. As a result, uncorrected Sun photometer measurements generally overestimate direct beam transmission and hence underestimate the AOD. This effect decreases with decreasing particle size as well as increasing wavelength. We computed this direct beam enhancement according to the formulations in *Russell et al.* [2004] for a half FOV of 1.85°, and multiplied 0.7 [see *Russell et al.*, 2004, Figure 3] to account for the smaller half FOV of the 4STAR sunlight collector, 1.4°. We found that the AOD underestimate was less than 0.003 for 80% of the observed 354 nm AOD in TCAP Phase 1, and less than 0.01 for 99%. The impact of diffuse light must be even smaller at longer wavelengths. On this basis, we chose not to correct the AOD for diffuse light.

[20] We obtain  $C_0$  through a refined Langley plot technique [*Schmid and Wehrli*, 1995]. The technique begins with measurements of sunlight over a wide range of air mass, followed by the adjustment for Earth-Sun distance

(equation (2)), Rayleigh scattering, and gas absorption (equation (4)). This is further followed by an iterative standard deviation based screening tailored for the Langley plot [*Schmid et al.*, 2003a, 2003b]. The resulting count rates in their natural logarithms plotted against the air mass are linearly extrapolated to air mass = 0 to yield  $C_0$ . In the July phase of TCAP, we applied this technique to high-altitude clear-sky observations aboard the G-1 on 22 July. Details are given in the Appendix A.

[21] The uncertainty in  $C_0$  dominated the overall uncertainties in the resulting AOD for the data presented here. The overall uncertainties are estimated to be ~0.01 at most wavelengths, slightly higher (~0.015) toward both ends of the measured spectrum (350 and 1660 nm). These uncertainty estimates include contributions associated with Sun tracking, dark counts stability, air mass calculation, Rayleigh scattering, gas absorption, and diffuse light, all mentioned above. Only at a few individual data points are these additional terms comparable with, or greater than, the  $C_0$  term (see Appendix A).

## 2.2. Nephelometer, Particle Soot Absorption Photometer (PSAP), f(RH)

[22] The G-1 was also equipped with instruments for in situ aerosol optical properties. We describe our treatment of the in situ data here, in preparation for comparison with the 4STAR measurements.

[23] The total light scattering coefficients at dry conditions were measured at three wavelengths (450, 550, and 700 nm) using the TSI nephelometer Model 3563. A sample flow of 30 liters per minute of air from the isokinetic inlet was maintained using a mass flow controller downstream of instrument. Data storage was performed at 1 Hz. The relative humidity of the sample was kept low (mean RH = 19%) by heating the sample by 2°C–5°C at the nephelometer inlet. The instrument was calibrated using three reference gases: zero air, sulfur hexafluoride, and carbon dioxide. Corrections for truncation and illumination were applied as per *Anderson and Ogren* [1998].

[24] The light absorption coefficients were measured using a Radiance Research particle soot absorption photometer (PSAP) at three wavelengths (462, 523, and 648 nm). The method is based on the Beer-Lambert law using the integrating plate technique in which the change in optical transmission of a filter caused by particle deposition on it is related to the light absorption coefficient of the deposited particles. *Bond et al.* [1999] found that the light absorption coefficient derived from PSAP is overestimated and multiple checks are needed to correct the data. The spot size calibrations were performed every day and flow was measured before, during, and after the campaign. All corrections were applied as per *Bond et al.* [1999].

[25] To measure the changes in total light scattering coefficients,  $\sigma$ , upon changes in relative humidity, or so-called f(RH), we ran three single-wavelength (525 nm) Aurora nephelometers Model 1000 at relative humidities near 45%, 65%, and 90%, respectively. Details of performance, calibration, and operations of this system are provided by *Pekour et al.* [2013]. They were calibrated using three gases, as described above for the TSI nephelometer. The f(RH) nephelometers use light-emitting diodes as light sources, and a 5 Lpm sample flow controlled by a critical orifice. The sample

is humidified or dried using multiple nafion tubes with 0.5 inch diameter. After the second phase of the TCAP campaign, we found that the RH sensors in all three Aurora nephelometers underestimated RH when compared to an accurate RH standard. The correction, by a slope of 1.5 and offset of  $-20$  percentage points at the highest RH, revealed that 30% of the data had been collected in saturated conditions ( $\text{RH} \geq 100\%$ ). Those data have been replaced with the nearest (in time) available data for this analysis. Also, the  $f(\text{RH})$  humidification unit failed on 18 July so we substitute 17 July data for that day. These two days saw similar single scattering albedo values in the lower troposphere. The losses of particles in the nafion tubes were characterized in the laboratory using ammonium sulfate and polystyrene latex spheres. Smoothly bent stainless tubes or conducting tubes were used for all instrument sample lines to minimize losses. The nafion units have particle loss of 2.5% per pair with maximum loss of  $<7.7\%$  in entire sampling lines. The system used three pairs of nafion tubes.

[26] Our study of vertically integrated particulate extinction in the ambient conditions (sections 3.2 and 3.3) demands that the three-point  $f(\text{RH})$  measurements be interpolated/extrapolated to the TSI nephelometer RH and the ambient RH (40–80%). We studied multiple fitting methods and assumptions to achieve this. In the end, we chose to fit a line through the  $f(\text{RH})$  measurements and to assume the slope of the line for RH between 30% and 100% and constant particulate scattering below 30%. We chose this method mainly because it achieves smaller fitting errors compared with the more common exponential curve fitting, i.e., linear regression on  $\log \sigma$  versus  $\log(1 - \text{RH}/100)$  coordinates, for the TCAP data. The exponential fitting yields rates of exponential increase,  $-\text{dln} \sigma / \text{dln}(1 - \text{RH}/100)$  commonly denoted  $\gamma$ , smaller ( $\sim 0.2$ ) than previously observed in the area ( $\sim 0.3$ – $0.5$ ) [Shinozuka *et al.*, 2007]. The linear method results in  $f(\text{RH})$  of 1.2–2.0 for the 11 columns studied in section 3.3, values similar to what a constant  $\gamma$  of 0.4 would yield.

[27] Humidified particles, being greater in size than dry ones, exhibit weaker wavelength dependence of light scattering. In other words, the changes in particulate light scattering upon humidity changes are proportionally greater at longer wavelengths in general. The 525 nm  $f(\text{RH})$  data need to be adjusted accordingly before being applied to other wavelengths. This is especially true for fine-mode particles with high Angstrom exponent ( $-\text{dlog} \sigma / \text{dlog} \lambda$  where  $\sigma$  is particulate scattering). Shinozuka *et al.* [2007, equation (2)] simulate the change in the wavelength dependence upon humidification of particles as a function of 540 nm  $f(\text{RH})$ :

$$\begin{aligned} A_{\text{amb}} = & \left( -0.022 * f(\text{RH})^3 + 0.16 * f(\text{RH})^2 - 0.47 * f(\text{RH}) + 1.3 \right) \\ & * (A_{\text{dry}} - 0.4) + 0.4 \end{aligned} \quad (5)$$

[28] According to this equation, a dry Angstrom exponent of 2.20 and  $f(\text{RH})$  of 1.2, for example, result in an ambient Angstrom exponent of 2.07. This means that 525 nm  $f(\text{RH})$  needs to be multiplied by 0.98, 1.01, and 1.04 for 450, 550, and 700 nm, respectively.

[29] To derive uncertainties in  $f(\text{ambRH})$  for the linear fitting method, we assumed a 3.5% relative random uncertainty in RH measurements in the Aurora nephelometers, a 5% random uncertainty in each Aurora nephelometer scattering measurement, and a 3.5% random uncertainty in the ambient RH records. The resulting relative error in  $f(\text{ambRH})$  is  $\sim 10\%$  at 80% ambient RH,  $\sim 5\%$  at 60% RH. We expanded the uncertainties to  $\sim 40\%$  to encompass the uncertainty ranges calculated for the exponential fitting method and a constant  $\gamma$  of 0.4.

[30] To calculate ambient extinction, the product of the adjusted  $f(\text{RH})$  and the dry scattering coefficients was added to the absorption coefficient interpolated/extrapolated to the TSI nephelometer wavelengths.

### 2.3. High Spectral Resolution Lidar (HSRL)-2

[31] During TCAP Phase 1, NASA Langley deployed the world's first airborne multiwavelength high spectral resolution lidar (HSRL). This instrument, called HSRL-2 (the second generation HSRL developed by NASA Langley), is an advanced version of the airborne HSRL-1 instrument [Hair *et al.*, 2008] that has acquired aerosol and cloud profiles on over 350 flights conducted on numerous field missions since 2006. In addition to implementing the HSRL technique at 532 nm as is also done with HSRL-1, the HSRL-2 system implements the HSRL technique at 355 nm to make independent, unambiguous retrievals of aerosol extinction and backscatter at both wavelengths. It also employs the standard backscatter technique at 1064 nm and is polarization sensitive at all three wavelengths. Consequently, HSRL-2 provides profile measurements of aerosol and cloud extinction and optical thickness via the HSRL technique at 355 and 532 nm, and profile measurements of aerosol and cloud backscatter and depolarization at 355, 532, and 1064 nm. The HSRL profile data are corrected to nadir based on the aircraft pitch and roll rather than implement a complex mechanical solution to achieve nadir pointing of the instrument. The instrument features an autonomous boresight system that insures the transmitter and receiver maintain coalignment during flight, similar to the boresight in the HSRL-1 system described in Hair *et al.* [2008, section E]. The vertical resolution of the backscatter coefficients and depolarization measurements is 15 m, and the temporal averaging is 10 s (about 1 km horizontal) [Rogers *et al.*, 2009]. The aerosol extinction profiles are computed at a vertical resolution of 150 m, and the temporal averaging is 60 s (about 6 km horizontal) [Rogers *et al.*, 2009]. The vertical and horizontal resolutions can be varied to suit different applications. During TCAP Phase 1, the HSRL-2 was deployed on the NASA Langley Research Center B-200 King Air which flew at an altitude of about 9 km. The flight patterns were conducted so that the G-1 flew within the HSRL-2 “curtains” enabling coincident and colocated measurements.

### 2.4. AERONET

[32] AERONET [Holben *et al.*, 1998] consists of automatic tracking Sun-sky radiometers located at  $\sim 400$  ground sites around the world. Used in this study are its level 2.0 AOD products, with typical time intervals of 2–15 min, at seven nominal wavelengths: 380, 440, 500, 675, 870, 1020, and 1640 nm, with ion-assisted deposition interference filters having FWHM band pass of 2 nm at 380 nm and 10 nm for all other wavelengths. For AERONET measurements, the



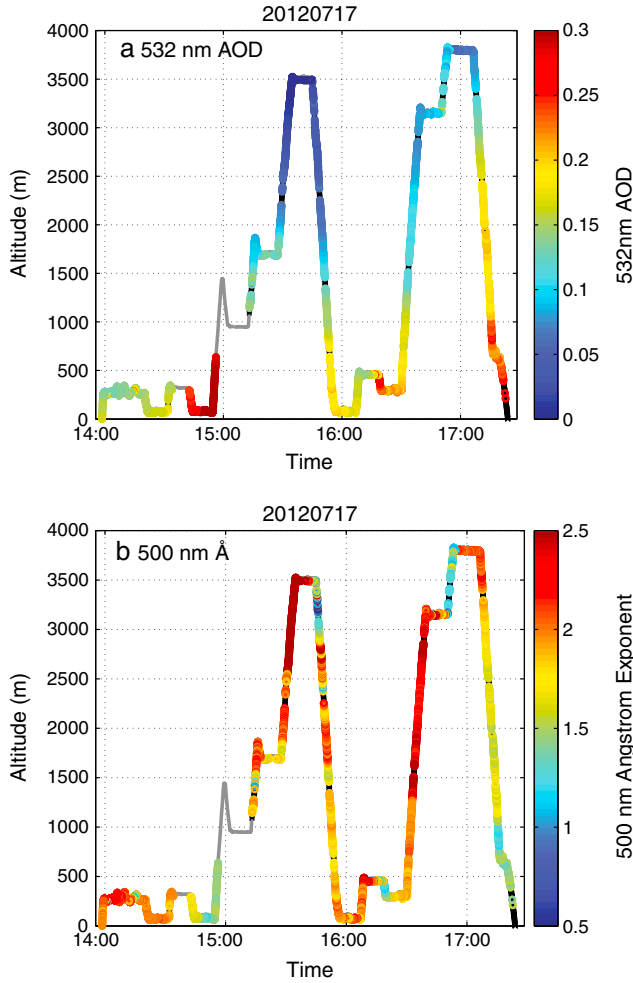


**Figure 3.** (a) The 4STAR AOD at 532 nm during the 17 July flight. As expected, the above-aircraft AOD, indicated by color, generally decreases with altitude ( $y$  axis) within each column. Data are interrupted by clouds, sky scanning, dark measurements, occasional motor and flight software issues, and operator errors. (b) The 4STAR Angstrom exponent at 500 nm.

uncertainty in AOD for field instruments is estimated as  $\sim 0.01$  to  $\sim 0.02$  at optical air mass of one, with the higher uncertainties in the ultraviolet channels (380 nm and 340 nm) [Eck *et al.*, 1999]. The FWHM FOV of the AERONET radiometers is  $\sim 1.2^\circ$ , resulting in biases due to forward-scattered diffuse radiation into the FOV much lower than 0.01, except for extremely high AOD and coarse mode dominated aerosols [Sinyuk *et al.*, 2012]. The cloud-screening and quality control procedures described for level 2 data by Smirnov *et al.* [2000] are applied. The locations of ARM Highlands Center and ARM Barnstable AERONET sites are marked as ground station and airport, respectively, in Figure 2.

### 3. Results

#### 3.1. Overview

[33] The 4STAR acquired AOD at 1 Hz in all flights of the first phase (July 2012) of TCAP campaign. The 532 nm AOD during the 17 July flight is shown in Figure 3a as an

example. As expected, the above-aircraft AOD, indicated by color, generally decreases with altitude within each column. The 1 Hz sample rate provides 5 m altitude resolution at an aircraft vertical speed of 1000 ft/min, and  $\sim 100$  m horizontal resolution during typical horizontal legs. Sun-tracking measurements are interrupted by clouds, sky scanning, dark measurements, occasional motor and flight software issues and operator errors.

[34] AOD are computed for some 500 wavelengths between 350 and 1660 nm outside strong gaseous absorption bands. These aerosol channels are marked black in Figure 4a. Most other channels of the two detectors, marked light blue and orange, respectively, are strongly affected by water vapor or oxygen absorption. The optical depth values shown for these channels, therefore, are not AOD. They and smaller spectral features are being investigated for gas retrievals [Segal-Rosenheimer *et al.*, 2013b].

[35] Angstrom exponent at 500 nm is shown in Figure 3b. For 4STAR, this parameter is calculated after applying a second-order polynomial fit in the  $\log(\text{AOD})$  versus  $\log \lambda$  space as  $-\text{dlog}(\text{AOD})/\text{dlog} \lambda$ . For the summer East Coast air mass, large Angstrom exponent values may be indicative of urban/industrial pollution, long-range transport of biomass-burning particles or both. Lower values indicate coarser particles such as aged organic and marine aerosols, and possibly the presence of thin clouds. The Angstrom values are relatively uncertain when the AOD is small. They are unrealistically high ( $>2.5$ ) for 6% of the cases shown here, most of them at 2500 m altitude or higher where the above-aircraft AOD was often  $<0.05$ .

#### 3.2. Comparison with Ground-Based Sun Photometers

[36] AOD comparisons with AERONET during fly-over events help us evaluate 4STAR's overall performance on the fast-moving platform. In addition, ground side-by-side comparisons provide more abundant data and serve as a test of radiometric calibration.

[37] Four flight segments satisfied criteria we require for comparison: 4STAR measurements made below 500 m altitude, within 2 km horizontally and 5 min of an AERONET level 2.0 AOD observation at the ground station. Of the 4STAR spectra in these distance and time windows for each fly-over event, those obtained in the lowest 30 m altitude flown (279–309 m), 15–34 of them per flight segment, are averaged and shown in Figure 4a.

[38] Of the two series of black dots in each panel, the upper one represents the AOD adjusted for an estimated below-aircraft contribution—the product of in situ ambient extinction (section 2.2) and the radar altitude measured onboard the G-1. This addition was calculated at the nephelometer wavelengths of 450, 550, and 700 nm. Its magnitude relative to the observed above-aircraft AOD, 4–12%, was then interpolated/extrapolated to other 4STAR wavelengths. The whole addition was incorporated as an additional uncertainty term for the full-column AOD which is shown for the 4STAR channel closest to each AERONET wavelength. For the AERONET AOD (red squares), the estimated uncertainties, 0.02 for 380 nm and 0.01 for all other wavelengths divided by the aerosol air mass factor, are shown by red bars.

[39] The root-mean-square (RMS) difference over the four cases in the full-column AOD between AERONET and 4STAR is 0.01 for wavelengths between 500 and 1020 nm,

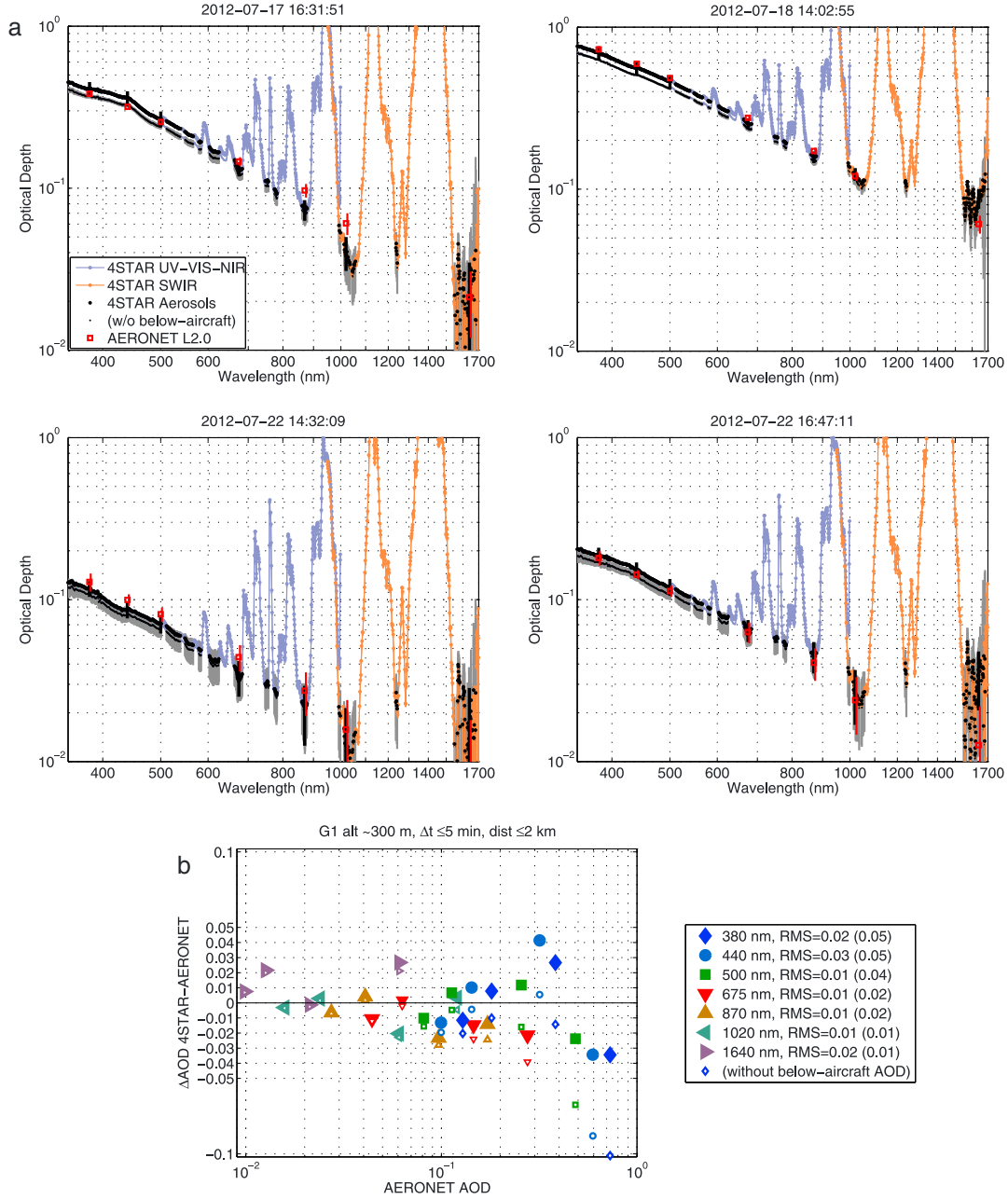


**Figure 4.** (a) The 4STAR optical depth spectra averaged for each of the four clear-sky fly-over events where the G-1 was within 2 km horizontally of the ground station and at  $\sim 300$  m altitude within 5 min of an AERONET measurement. Aerosol channels are marked black. Light blue and orange dots indicate the channels of the two detectors that are affected by strong water vapor and oxygen absorption. Grey bars represent the uncertainty range estimated for the above-aircraft AOD. The black vertical bars put near AERONET channels represent the uncertainty range estimated for the full-column AOD including the below-aircraft contribution. (b) AOD difference between the 4STAR aboard the G-1 and the AERONET on the ground station. Smaller markers and the RMS values in the parentheses are for the 4STAR observation before an estimated below-aircraft AOD was added.

0.02 at 380 and 1640 nm, and 0.03 at 440 nm. This is noted in Figure 4b in the legend, accompanied by the preadjustment values in parentheses. The below-aircraft adjustment reduces the RMS difference at all wavelengths except 1640 nm. Bias, defined as the mean of the differences at each wavelength over the colocation events, is between  $-0.01$  and  $+0.01$  at all wavelengths. The RMS difference and bias are

also presented in Table 1 together with the results of linear least squares bisector regression. The AOD differences are partly explained by the variability in the ambient aerosols between the two instruments. When they were especially close to each other in one of the four events—within 1 km horizontally and 2.5 min of each other—the AOD difference was as small as 0.003 at most wavelengths. Meanwhile, the variability

**Table 1.** Full-Column AOD Comparisons

$\lambda$ (nm) <sup>a</sup>	n	RMS	Bias	Mean( $x$ )	Mean( $y$ )	R <sup>2</sup>	Slope	Intrc.
<i>y = 4STAR on G-1<sup>b</sup>, x = AERONET at Ground Station</i>								
380	4	0.99	0.95	0.01	0.02	−0.00	0.36	0.35
440	4	0.98	0.95	0.01	0.03	+0.00	0.29	0.29
500	4	0.99	0.95	0.01	0.01	−0.00	0.23	0.23
675	4	1.00	0.93	−0.00	0.01	−0.01	0.13	0.12
870	4	0.98	0.91	−0.00	0.01	−0.01	0.08	0.07
1020	4	0.95	1.05	−0.01	0.01	−0.00	0.06	0.05
1640	4	0.90	1.39	0.00	0.02	+0.01	0.03	0.04
<i>y = 4STAR at Airport<sup>c</sup>, x = AERONET at Airport</i>								
380	21	1.00	1.04	−0.03	0.02	−0.01	0.28	0.29
440	21	1.00	1.06	−0.03	0.02	−0.01	0.23	0.23
500	21	1.00	1.04	−0.02	0.02	−0.02	0.20	0.19
675	21	1.00	1.08	−0.01	0.01	−0.00	0.10	0.11
870	21	0.99	1.03	−0.02	0.01	−0.01	0.08	0.07
1020	23	0.94	1.09	0.01	0.01	+0.01	0.04	0.05
1640	23	0.75	0.96	0.01	0.01	+0.01	0.03	0.04
<i>y = 4STAR at Moffett Field, x = AATS-14 at Moffett Field</i>								
354	6365	0.99	0.98	−0.01	0.01	−0.01	0.08	0.07
380	6365	0.99	0.90	0.00	0.01	−0.00	0.08	0.07
452	6365	0.98	0.87	0.00	0.01	−0.01	0.06	0.05
500	6365	0.98	0.89	−0.00	0.01	−0.01	0.06	0.05
520	6365	0.98	0.88	−0.00	0.01	−0.01	0.05	0.04
605	6365	0.97	0.83	−0.00	0.01	−0.01	0.04	0.03
675	6365	0.94	0.81	−0.00	0.01	−0.01	0.04	0.03
781	6365	0.96	0.80	0.00	0.00	−0.00	0.03	0.03
865	6365	0.93	0.81	0.00	0.01	−0.00	0.03	0.03
1019	6365	0.87	0.74	−0.01	0.02	−0.02	0.03	0.01
1236	6365	0.88	0.78	0.01	0.01	+0.01	0.01	0.02
1559	6365	0.70	0.70	−0.01	0.01	−0.01	0.02	0.00

<sup>a</sup> $\lambda$  is the wavelength, n is the number of comparison cases, R<sup>2</sup>, Slope and intrc. are the coefficient or determination, slope and intercept, respectively, of the linear least squares bisector regression, RMS is the root mean square, and bias is mean( $y-x$ ).

<sup>b</sup>The 4STAR above-aircraft AOD was measured at ~300 m altitude within 2 km horizontally and  $\pm 5$  min of the AERONET observation and augmented for the below-aircraft contributions.

<sup>c</sup>The number of samples varies with wavelength because the UV-VIS-NIR detector did not collect data for a brief time period before the 25 July flight while the SWIR detector did.

among the 4STAR measurements was as small as 1% of the average for each of the four cases.

[40] Ground-based comparisons show similar results. The 4STAR was operated intermittently alongside another AERONET instrument while the G-1 was parked at the Barnstable Airport. Example of time series at select wavelengths are plotted in Figure 5a. The 4STAR AOD were averaged for  $\pm 5$  min time window for each of the 23 comparison cases over 4 days. The RMS differences of 4STAR versus AERONET (Figure 5c and Table 1) are 0.01–0.02 like the aircraft-to-ground comparisons, though at 500 nm, it is twice as large.

[41] Additional ground side-by-side comparisons were made about a month after the July 2012 TCAP Phase 1 to further evaluate the calibration stability. As a reference for this test, we used AATS-14 that had been calibrated at the Mauna Loa Observatory in May 2012 following our standard procedure (see section 2.1 for references). Four-hour clear-sky observations on the rooftop of NASA Ames Research Center Building 245 in Moffett Field, California, on 22 August 2012 (select wavelengths shown in Figure 5b) show AOD differences near 0.01 at most of AATS-14's 12 channels (Figure 5c and Table 1; the missing two channels

are 941 nm affected by water vapor and 2139 nm beyond 4STAR's spectral range). The azimuthal position of the FORJ impact at the time of these measurements is unknown; without this effect, the AOD differences could be greater or smaller by up to 0.008. At near-infrared channels (e.g., 1559 nm) where the dark counts of 4STAR are relatively close to the total photon counts, the 4STAR AOD are noisier than both the AATS AOD at the same wavelengths and the 4STAR AOD at shorter wavelengths (Figure 5b). Overall, 4STAR's once-per-second measurements track the 3 s average AATS AOD, and both show identical fine features in the time series.

### 3.3. Comparison With Airborne Instruments

[42] Here we compare two sets of altitude-resolved optical measurements with 4STAR. This needs to be done in terms of layer AOD—the fraction of AOD that corresponds to the range of altitudes flown by the aircraft.

[43] The calculation of the layer AOD begins with identifying spiral ascents and descents. The time bounds of each spiral were shortened to the point where both 4STAR and in situ instruments provided valid data in absence of clouds, dark measurements, and instrument issues. In total, there are 11 spirals on 7 days that are at least 1 km deep. They span about 10 km diameter each.

[44] The 4STAR layer AOD is given as the difference in the observed AOD between the bottom and the top of each profile (Figure 6a, blue dots). The layer AOD was interpolated to the wavelengths affected by strong gas absorptions by means of a second-order polynomial fit (blue curve in the figure). The fit provides reasonable estimates of 700 and 1064 nm layer AODs: Its discrepancy from the observed layer AOD is  $<0.01$  at 684 nm (the aerosol channel closest to 700 nm) and 1057 nm (that closest to 1064 nm) for the profiles studied here.

[45] The observed 450 and 550 nm layer AOD and the interpolated 700 nm layer AOD are plotted on the  $x$  axis of Figure 6b. Colored horizontal bars indicate the uncertainty intrinsic to the instrument, which arose largely from the FORJ (section 2.1), estimated from the bottom and top measurements after Redemann *et al.* [2003, equation (6)]. The grey bars associated with the 450 and 550 nm data points are a measure of horizontal variability, spanning the center two thirds of 4STAR observations at the bottom of each column over the traveled area in or near the spirals. These bars are considerably shorter than for central Canada's forest fire smoke [Shinozuka *et al.*, 2011], indicating less spatial variability in the current study. Plotted on the  $y$  axis is the in situ layer AOD or the vertical integral over the same layers of the  $f(\text{RH}) \times \text{neph} + \text{PSAP}$  extinction coefficients (section 2.2).

[46] The in situ minus 4STAR RMS differences in layer AOD are 0.03, 0.02, and 0.02 at 450, 550, and 700 nm, respectively (Figure 6c and Table 2). The biases are +0.02, +0.01, and +0.01, respectively. The impact of the wavelength dependence of the humidity response on these statistics is negligible; they are virtually the same if the 525 nm  $f(\text{RH})$  is applied at all wavelengths. Note that the 4STAR layer AOD are highly uncertain when  $<0.01$ , as was the case in the 25 July 16:32:35 to 16:40:49 profile. This is marked by long uncertainty bars in Figure 6b and by the unrealistic increases with increasing wavelength (Figures 6b and 6c).



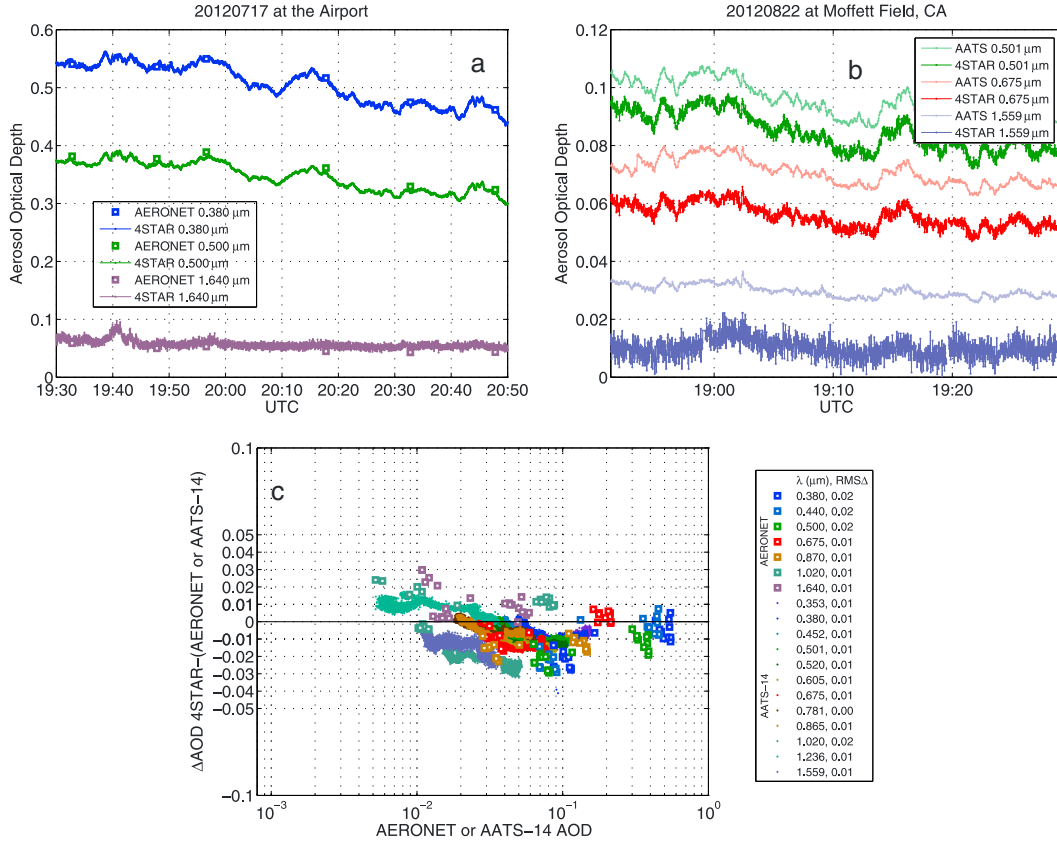


**Figure 5.** Example time series of 4STAR measurements compared (a) with AERONET at the Barnstable Airport and (b) with AATS-14 at Moffett Field. (c) AOD difference between the 4STAR and each ground-based instrument.

[47] Similar comparisons with the vertical integral of HSRL-2 extinction measurements (Figure 6d) found RMS differences of 0.01, 0.01, and 0.02 at 355, 532, and 1064 nm, respectively (Figure 6e and Table 2), and biases of 0, +0.01, and +0.01, respectively. These statistics are for six spirals on 4 days where the lidar measurements were made within 10 km horizontally and  $\pm 15$  min of the bottom of the G-1 spiral. The 4STAR layer AOD was directly observed at 355 and 532 nm; the 1064 nm values are the result of interpolation. The random uncertainties in the HSRL-2 layer AOD (vertical bars in Figure 6d) are based on the signal level at the top and the bottom of the layer [Hair *et al.*, 2008] after the technique developed by Liu *et al.* [2006]. The random uncertainty for the 1064 nm layer AOD is not estimated at this point. The HSRL-2 extinction and AOD measurements at 355 and 532 nm are derived using the HSRL technique which does not require assumptions or additional information relating aerosol backscatter to extinction. Therefore, these measurements are significantly more accurate than extinction measurements made with standard elastic backscatter lidar. Potential sources of systematic error in the layer AOD and extinction retrievals (not included in the plotted error bars) include the atmospheric state parameters, the laser and receiver spectral stability, and internal calibrations that are performed routinely during flight. These sources are discussed quantitatively for the 532 nm measurements by Hair *et al.* [2008]. The 355 nm layer AOD products from the airborne HSRL-2 instrument

are a new research product and are presented here for the first time. A complete assessment of the calibration errors has not yet been completed. In contrast to the 355 nm and 532 nm channels, the 1064 nm channel does not use the HSRL technique. Instead, aerosol extinction at 1064 nm is calculated using the aerosol backscatter measurements and an estimate of the aerosol extinction/backscatter ratio ( $S_a$ ). The  $S_a$  estimate is obtained using an inference of aerosol type derived from the full suite of intensive aerosol parameters measured at 532 nm and 1064 nm [see Burton *et al.*, 2012]. The layer AOD was then determined from the integrated extinction within the layer.

### 3.4. Extinction Profiles

[48] As an application of the airborne Sun photometry, vertical profiles of AOD can be differentiated with respect to altitude to yield extinction profiles. This technique works when the atmospheric constituents are distributed homogeneously over the horizontal extent of the slant path toward the Sun and stable over the measurement time period. An example is shown in Figure 7. To the 4STAR 550 nm AOD profile observed between 20:08:40 and 20:26:00 on 9 July 2012 (Figure 7a, black curve), we applied 50 m altitude bin averaging and fitted a spline curve (red) after Schmid *et al.* [2006]. The spline smoothing makes the vertical resolution degraded from 50 m, perhaps to  $\sim 300$  m for this profile, the degree of degradation being sensitive to the shape of profile. We then differentiated the result with respect to

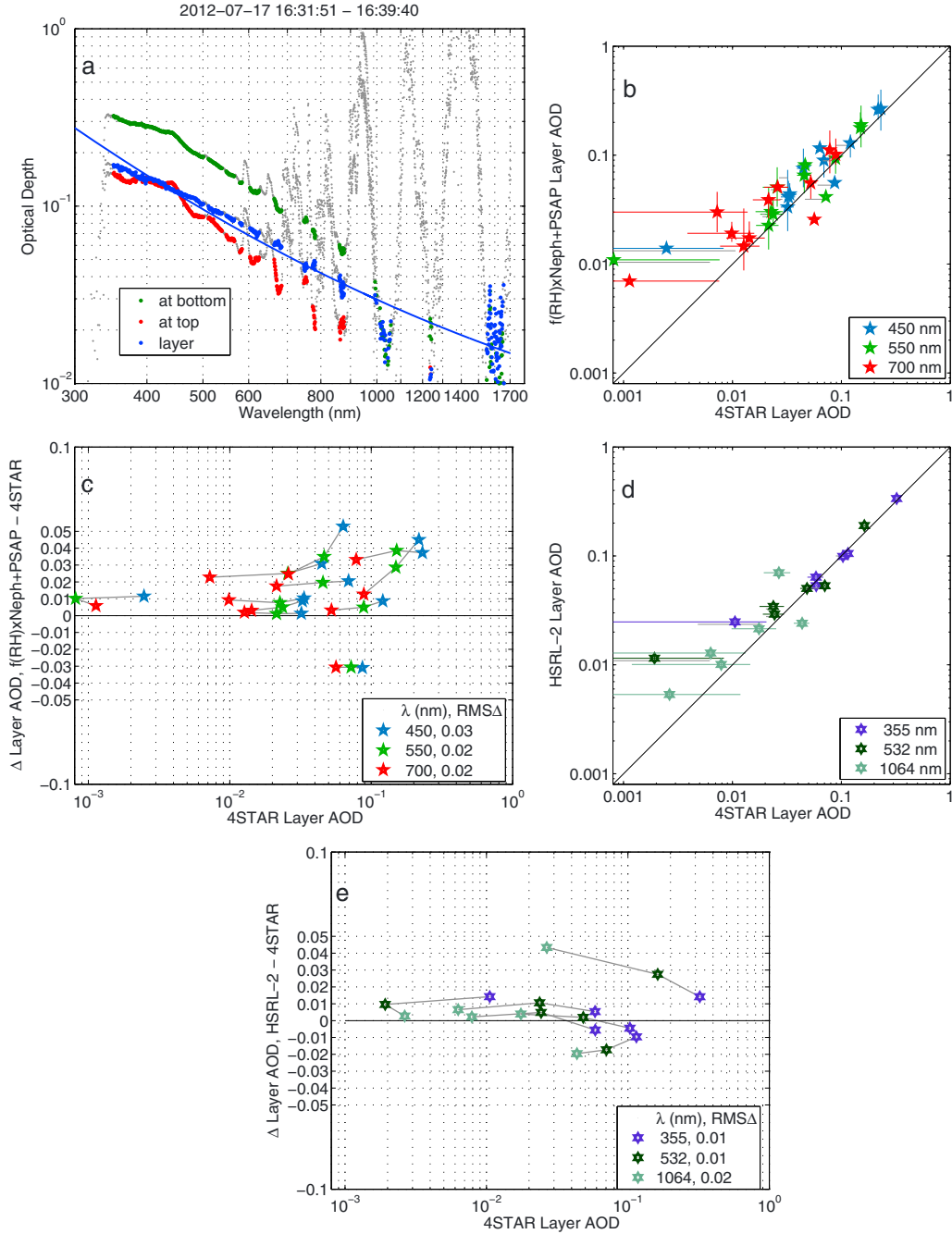


**Figure 6.** (a) The 4STAR AOD at the bottom and top of the G-1 spiral ascent made on 22 July 16:50:10 to 17:01:49. Their difference, the layer AOD, is also shown together with a second order polynomial fit. (b) Layer AOD comparison with coincident airborne in situ measurements from the G-1. (c) The layer AOD differences (in situ—4STAR) compared with the 4STAR layer AOD. Each set of the extinction measurements is connected with grey lines. (d) Layer AOD comparison with coincident airborne HSRL-2 measurements from the B-200. (e) The layer AOD differences (HSRL-2—4STAR).

altitude to yield the extinction coefficient (Figure 7b, red curve). This compares well with the coincident in situ extinction (blue) with an RMS difference of 2.1 inverse megameter ( $\text{Mm}^{-1}$ ) or 14% of the average. Some of the differences are due simply to differences in the vertical resolution and the smoothing applied to the 4STAR data. The same smoothing and differentiation, once applied to all aerosol channels, yield vertically resolved hyperspectral extinction

coefficients (Figure 7c). The differentials are erroneous in near-infrared wavelengths where the signal-to-noise ratio of the 4STAR measurements is generally low.

#### 4. Discussion

[49] The good agreement with AERONET (section 3.2) attests to the credibility of 4STAR. The discrepancies due

**Table 2.** Layer AOD Comparisons

$\lambda$ (nm) <sup>a</sup>	n	RMS	Bias	Mean (x)	Mean (y)	R <sup>2</sup>	Slope	Intrc.
<i>y = Neph, PSAP, and f(RH) on G-1, x = 4STAR on G-1</i>								
450	11	0.94	1.16	0.00	0.03	+0.02	0.08	0.10
550	11	0.91	1.18	0.00	0.02	+0.01	0.06	0.07
700	11	0.77	1.16	0.00	0.02	+0.01	0.03	0.04
<i>y = HSRL2 on B-200, x = 4STAR on G-1</i>								
355	6	0.99	1.03	-0.00	0.01	+0.00	0.11	0.11
532	6	0.96	1.13	-0.00	0.01	+0.01	0.06	0.06
1064	6	0.27	1.85	-0.01	0.02	+0.01	0.02	0.02

<sup>a</sup> $\lambda$  is the wavelength, n is the number of comparison cases, R<sup>2</sup>, Slope and intrc. are the coefficient of determination, slope, and intercept, respectively, of the linear least squares bisector regression, RMS is the root mean square, and bias is mean(y-x).

to 4STAR errors must be even smaller than the apparent differences (mostly 0.01–0.02), because the latter also include the AERONET error ( $\sim 0.01$ ) and the atmospheric variation in horizontal distance (2 km) and time ( $\pm 5$  min). In fact, in one event where the two instruments were within 1 km and  $\pm 2.5$  min of each other, the AOD difference was as small as 0.003 at most wavelengths. The agreement implies that, in environmental conditions similar to the July phase of TCAP and with the aid of in situ instruments, 4STAR can usefully extend the capabilities of land-based Sun photometers in validating satellite remote-sensing products (over oceans and other regions without ground stations) and supporting suborbital observations (by flying with other instruments). The agreement with AATS-14 further suggests calibration stability over the course of 1 month.

[50] All this was achieved despite the difficulties faced in calibration. We substituted a new UV-VIS-NIR spectrometer into 4STAR just before the TCAP deployment, following our discovery of malfunctions in the original spectrometer, which had undergone extensive premission characterization. The premission calibrations did not hold for the new spectrometer. Postmission calibrations with the July 2012 setup were precluded beyond the 22 August test by the urgent need for the replacement of parts and subsequent characterizations. The lack of repeated calibrations is partly responsible for estimated uncertainties that are themselves highly uncertain. But what dominates the estimated uncertainties, 0.01 at most wavelengths, is the impact of unpredictable changes, up to  $\pm 0.8\%$  as demonstrated on high-altitude circle legs, in light transfer efficiency of the FORJ (see section 2.1 and Appendix A). Related optical parts were later altered and the throughput changes are being characterized.

[51] Indeed, while 4STAR performed well for its first airborne mission, more characterizations need to be made. Performance has not been rigorously evaluated under higher air mass factors (lower Sun), on bumpier flights or in colder and more humid air. The detector stability over months remains to be tested. Dunagan *et al.* [2013] provide information on error sources and their magnitudes, along with discussion of calibration and correction strategies to improve measurement accuracy when deterministic error characterization is possible.

[52] In the meantime, advantages of the high temporal resolution (1 Hz) manifested themselves as high spatial resolution,

5 m vertical and  $\sim 100$  m horizontal, during the airborne measurements (section 3.1). The 4STAR and its predecessors AATS-6 and AATS-14, all tailored for fast-moving platforms, detect light simultaneously at all wavelengths, unlike conventional ground-based Sun photometers that switch from one filter to another. The ability to observe AOD at every  $\sim 100$  m is increasingly useful, as science surrounding air quality [Hoff and Christopher, 2009] and aerosol-cloud interaction [Redemann *et al.*, 2009; McComiskey and Feingold, 2012] demands data at ever finer scales. Better characterization of horizontal variability of aerosol loading also helps interpretation of satellite data and its use in combination with other spaceborne and suborbital observations, as well as optimization of ground-based long-term monitoring stations [Shinozuka and Redemann, 2011]. The high frequency of 4STAR is advantageous on the ground too. It can record fine features in AOD time series, like the example shown in Figure 5b.

[53] The 4STAR's wide spectral range and ability to observe AOD at various altitudes uniquely enabled comparison with the HSRL-2 lidar layer AOD. A high level of consistency was demonstrated at 532 nm, with an RMS difference over the six profiles of 0.01 (Figures 6d and 6e). This success is partly attributable to the HSRL technique that enables extinction and backscattering to be characterized independently. At 1064 nm where extinction was not measured but estimated from the backscattering, the RMS difference was greater even in the absolute terms (0.02), in spite of the smaller layer AOD values.

[54] The 4STAR layer AOD was compared with the in situ measurements as well. Linear regression resulted in a negligible intercept but a slope 16–18% greater than unity at each wavelength (Table 2). This represents a level of agreement somewhat inferior to a recent study in the U.S. East Coast [Ziemba *et al.*, 2013]. The RMS differences were 0.02–0.03 and the biases were between 0 and +0.01. For some individual cases, the differences were as large as 0.04 at 550 nm. These individual cases and the positive bias, the latter of which marks a departure from some previous studies [Schmid *et al.*, 2006; Shinozuka *et al.*, 2007], call for verifications through similar comparisons after 4STAR and the in situ instruments are better calibrated and characterized.

[55] These comparisons of layer AOD are facilitated by the fact that 4STAR data do not require adjustments for humidity difference or for loss of coarse particles in a sample inlet. The same features facilitate the derivation of ambient extinction profiles (section 3.4). This capability is invaluable, as few airborne instruments other than HSRL systems are capable of directly measuring extinction coefficient and hyperspectral ones hitherto nonexistent.

## 5. Conclusions

[56] AOD is an important measure of atmospheric particles. The column-integrated light extinction is widely used to study their effects on the climate and air quality as well as to evaluate observations from Earth monitoring satellites.

[57] The new Sun photometer, 4STAR, demonstrated its ability to accurately measure AOD during the TCAP experiment. The results from both airborne and ground-based operations fell mostly within 0.01–0.02 of the ground-based AERONET AOD observations. The differences are due to both atmospheric variations and combined instrument errors.

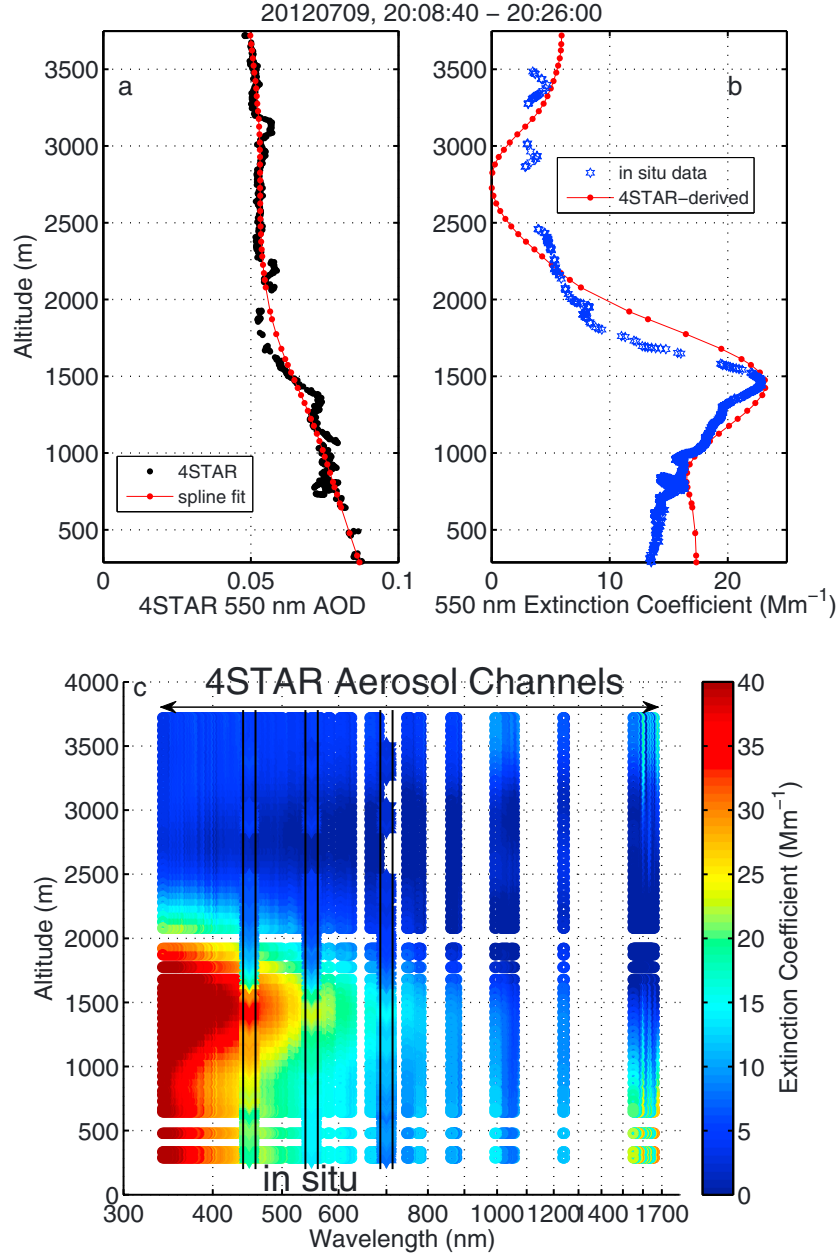


**Figure 7.** Derivation of extinction coefficients for the vertical profile flown on 9 July 2012. (a) The measured 550 nm AOD and a spline fit. A spline fit parameter of 0.90 was applied to 50 m altitude bin averages. (b) Ambient extinction coefficient derived from the smoothed AOD profile (red), compared with the coincident in situ observation (blue). (c) The derived 4STAR extinction coefficient at all wavelengths unaffected by strong gas absorption. The 450, 550, and 700 in situ data are superimposed. In situ data are not available at any of the three wavelengths at some altitudes above 2500 m.

Although 4STAR's performance remains to be tested under different types of environment over a longer term, and some optical parts leave room for improvement, the favorable intercomparisons during its first airborne mission attest to its credibility.

[58] The 4STAR has many advantages over other AOD instruments, as our TCAP deployment showed. The airborne instrument can be used to conduct research over regions with few stations such as oceans, swiftly chasing air masses of interest as they evolve, together with other airborne instruments. The simultaneous light detection across all wavelengths

eliminates the need for rotating filters and achieves high temporal and spatial resolution. The ability to observe AOD at various altitudes is invaluable, not least for comparison with accompanying in situ and lidar extinction measurements. In addition to these features adopted from its predecessors AATS-14 and AATS-6, 4STAR uniquely provides data over continuous spectral channels. It is also capable of observing the sky and clouds and delivering column density of some trace gases, which are topics of future papers. We expect that a variety of research projects related to aerosols can put these features to good use.

## Appendix A: Calibration Technique

[59] Radiometric calibration of a Sun photometer means gauging what the instrument response would be at zero air mass. We achieve this by extrapolating from the responses measured under a wide range of air mass factors. This so-called Langley plot technique [Schmid and Wehrli, 1995] requires a stable atmospheric optical depth and instrument performance for the duration of the measurements, usually hours after sunrise or before sunset.

[60] This technique has been applied to 6 km altitude flight legs flown on 22 July 21:14 to 23:28 UTC or 17:14 to 19:28 local U.S. East Coast summer time. The natural logarithm of the count rate adjusted for the aerosol component (defined by equation (4)),  $\ln C_p$  (Figure A1, grey dots), approximately forms a straight line against the aerosol air mass factor,  $m_p$ , as expected from equation (1) (section 2.1). But these original data are noisy. The magnitude of noise, as measured by the  $\pm 1$  standard deviation range of all data points, is  $\pm 0.8\%$ . The noise partly reflects changes in atmospheric constituents, besides the occasional blockage by an antenna aircraft wire and possible clouds.

[61] But the noise is predominantly due to the variations in the light transmission efficiency of the FORJ. Previous tests with a stable light source and with sunlight, the latter alongside AATS-14, both indicate that the throughput depends largely on the azimuthal position of the instrument head relative to its body. The magnitude of this variation was typically near  $\pm 0.8\%$ . Unfortunately, the angular dependence itself changed unpredictably, sometimes only after a few days of stability. (The latter issue was significantly improved in late 2012).

[62] The lack of repeatability made the correction of the FORJ impact impractical in the field. This led us to seek the calibration that represents the average FORJ sensitivity. Since the standard screening process [Schmid et al., 2003a, 2003b] turned out to accept data points positioned on the upper part of the FORJ sensitivity (Figure A1, green dots), we shifted the resulting regression line (solid line) downward by 0.8% (dashed line).

[63] Our uncertainty estimate for  $C_0$  includes  $\pm 0.8\%$  over the entire wavelengths to reflect the FORJ instability. This translates into an AOD uncertainty of  $\pm 0.008/m_p$  where  $m_p$ , the air mass factor for aerosols, is between 1.08–1.40 for most of the TCAP Phase 1 science flights.

[64] Apart from the FORJ impact, the impact of the nonlinearity is probably close to  $\pm 0.6\%$ . The air mass range between 7.5 and 11.1 of the 22 July airborne Langley plot saw a relatively stable azimuthal angle of the instrument as the airplane traveled straight. The linear regression applied for the data in this range and extended to zero air mass (black dots) results in a 0.6% greater  $C_0$  than the value obtained from the entire filtered data.

[65] Uncertainty also arises from changes in the detector performance. We deduced the magnitude of this component—the variability, not the  $C_0$  values themselves—from our two airborne Langley results during the February 2013 phase of TCAP. The magnitude is near  $\pm 0.5\%$  for most wavelengths. This detector change component may or may not explain the nonlinearity.

[66] With uncertainty components combined as a sum of squares, the overall AOD uncertainties are near  $\pm 1\%$  at most

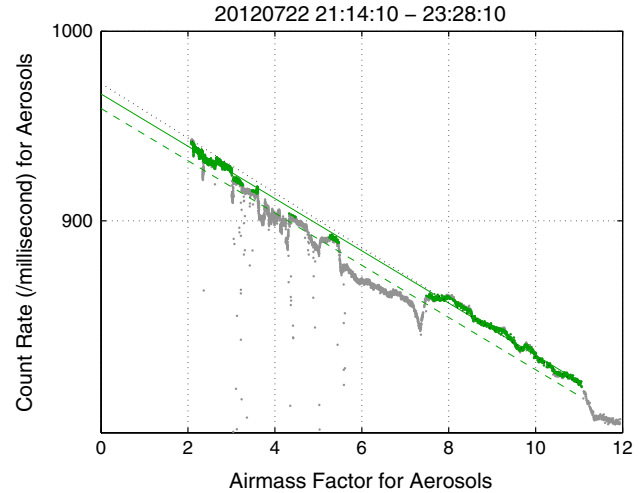


**Figure A1.** Langley plot from the 22 July evening flight at 6 km altitude. The count rate on the y axis is already adjusted for the effects of atmosphere and absorption by  $O_3$ ,  $NO_2$ , and  $O_2-O_2$ . Effects of aircraft wire crossing and possible cirrus clouds as well as some other data points were screened out (grey dots) after the iterative method described in Schmid et al. [2003a, 2003b]. A linear regression was applied to the remaining data points (green). The result (solid line) was shifted down by 0.8% (dashed) to account for the impact of FORJ. The black dots represent the linear regression applied to the air mass range between 7.5 and 11.1 and extended to 0.

wavelengths, which translates into  $\pm 0.01/m_p$  AOD uncertainties. They are slightly higher ( $\sim \pm 1.5\%$  in  $C_0$  or  $\pm 0.015/m_p$  AOD) toward both ends of the wavelengths (350 and 1660 nm).

[67] **Acknowledgments.** We would like to thank the DOE ARM aerial facility staff Mike Hubbell, Bill Svancara, Dick Hone, Jason Tomlinson, and Gene Dukes for carrying out the G-1 research flights; the NASA Langley King Air flight crew Mike Wusk, Dale Bowser, Dean Riddick, Scott Sims, Rick Yasky, Greg Slover, and Leslie Kagey for their outstanding work supporting the B-200 flights and measurements; Meloë Kacenelenbogen for her contribution during the calibration of AATS-14; and Qin Zhang for assistance with preparing the figures. The 4STAR hardware and science algorithm development were funded by the NASA Radiation Science Program, the Ames Instrument Working Group, and the NOAA Office of Global Programs. Further maturation of 4STAR as well as the participation of 4STAR in TCAP and subsequent analyses was funded by the DOE ARM program. Analysis and interpretation of data collected on board the G-1 were supported by the DOE ARM and DOE Atmospheric System Research (ASR) Programs.

## References

- Anderson, T. L., and J. A. Ogren (1998), Determining aerosol radiative properties using the TSI 3563 integrating nephelometer, *Aerosol Sci. Technol.*, 29, 57–69.
- Asseng, H., T. Ruhtz, and J. Fischer (2004), Sun and aureole spectrometer for airborne measurements to derive aerosol optical properties, *Appl. Opt.*, 43(10), 2146–2155.
- Bogumil, K., et al. (2003), Measurements of molecular absorption spectra with the SCIAMACHY pre-flight model: Instrument characterization and reference data for atmospheric remote-sensing in the 230–2380 nm region, *J. Photochem. Photobiol., A*, 157(2), 167–184, doi:10.1016/S1010-6030(03)00062-5.
- Bond, T. C., T. L. Anderson, and D. Campbell (1999), Calibration and intercomparison of filter-based measurements of visible light absorption by aerosols, *Aerosol Sci. Technol.*, 30, 582–600.
- Bucholtz, A. (1995), Rayleigh-scattering calculations for the terrestrial atmosphere, *Appl. Opt.*, 34, 2765–2773.
- Burton, S. P., R. A. Ferrare, C. A. Hostetler, J. W. Hair, R. R. Rogers, M. D. Obland, C. F. Butler, A. L. Cook, D. B. Harper, and K. D. Froyd



- (2012), Aerosol classification using airborne high spectral resolution lidar measurements—Methodology and examples, *Atmos. Meas. Tech.*, 5(1), 73–98, doi:10.5194/amt-5-73-2012.
- Dunagan, S., R. Johnson, J. Zavaleta, P. Russell, B. Schmid, C. Flynn, J. Redemann, Y. Shinozuka, J. Livingston, and M. Segal-Rosenheimer (2013), Spectrometer for Sky-Scanning Sun-Tracking Atmospheric Research (4STAR): Instrument technology, *Remote Sens.*, 5(8), 3872–3895, doi:10.3390/rs5083872.
- Eck, T. F., B. N. Holben, J. S. Reid, O. Dubovik, A. Smirnov, N. T. O'Neill, I. Slutsker, and S. Kinne (1999), Wavelength dependence of the optical depth of biomass burning, urban, and desert dust aerosols, *J. Geophys. Res.*, 104(D24), 31,333–31,349, doi:10.1029/1999JD900923.
- Ferrare, R., et al. (2000), Comparisons of LASE, aircraft, and satellite measurements of aerosol optical properties and water vapor during TARFOX, *J. Geophys. Res.*, 105(D8), 9935–9947, doi:10.1029/1999JD901201.
- Ferrare, R., et al. (2006), Evaluation of daytime measurements of aerosols and water vapor made by an operational Raman lidar over the Southern Great Plains, *J. Geophys. Res.*, 111, D05S08, doi:10.1029/2005JD005836.
- Hair, J. W., C. A. Hostetler, A. L. Cook, D. B. Harper, R. A. Ferrare, T. L. Mack, W. Welch, L. R. Izquierdo, and F. E. Hovis (2008), Airborne high spectral resolution lidar for profiling aerosol optical properties, *Appl. Opt.*, 47(36), 6734–6752.
- Hoff, R. M., and S. A. Christopher (2009), Remote sensing of particulate pollution from space: Have we reached the promised Land?, *Journal of the Air & Waste Management Association*, 59(6), 645–675, doi:10.3155/1047-3289.59.6.645.
- Holben, B. N., et al. (1998), AERONET—A federated instrument network and data archive for aerosol characterization, *Remote Sens. Environ.*, 66(1), 1–16.
- Karol, Y., D. Tanré, P. Goloub, C. Vervaeke, J. Y. Balois, L. Blarel, T. Podvin, A. Mortier, and A. Chaikovsky (2013), Airborne Sun photometer PLASMA: Concept, measurements, comparison of aerosol extinction vertical profile with lidar, *Atmos. Meas. Tech.*, 6(9), 2383–2389, doi:10.5194/amt-6-2383-2013.
- Liu, Z., W. Hunt, M. Vaughan, C. Hostetler, M. McGill, K. Powell, D. Winker, and Y. Hu (2006), Estimating random errors due to shot noise in backscatter lidar observations, *Appl. Opt.*, 45(18), 4437–4447.
- Livingston, J., et al. (2000), Shipboard sunphotometer measurements of aerosol optical depth spectra and columnar water vapor during ACE-2, and comparison with selected land, ship, aircraft, and satellite measurements, *Tellus B*, 52(2), 594–619, doi:10.1034/j.1600-0889.2000.00045.x.
- Livingston, J., et al. (2003), Airborne Sun photometer measurements of aerosol optical depth and columnar water vapor during the Puerto Rico Dust Experiment and comparison with land, aircraft, and satellite measurements, *J. Geophys. Res.*, 108(D19), 8588, doi:10.1029/2002JD002520.
- Livingston, J. M., et al. (2005), Retrieval of ozone column content from airborne Sun photometer measurements during SOLVE II: Comparison with coincident satellite and aircraft measurements, *Atmos. Chem. Phys.*, 5(8), 2035–2054, doi:10.5194/acp-5-2035-2005.
- Livingston, J., et al. (2007), Comparison of water vapor measurements by airborne Sun photometer and near-coincident in situ and satellite sensors during INTEx/ITCT 2004, *J. Geophys. Res.*, 112, D12S16, doi:10.1029/2006JD007733.
- Livingston, J. M., B. Schmid, P. B. Russell, J. R. Podolske, J. Redemann, and G. S. Diskin (2008), Comparison of water vapor measurements by airborne Sun photometer and diode laser hygrometer on the NASA DC-8, *J. Atmos. Oceanic Technol.*, 25(10), 1733–1743, doi:10.1175/2008JTECHA1047.1.
- Livingston, J. M., et al. (2009), Comparison of aerosol optical depths from the Ozone Monitoring Instrument (OMI) on Aura with results from airborne sunphotometry, other space and ground measurements during MILAGRO/INTEx-B, *Atmos. Chem. Phys.*, 9(18), 6743–6765.
- Matsumoto, T., P. Russell, C. Mina, W. Van Ark, and V. Banta (1987), Airborne tracking Sunphotometer, *J. Atmos. Oceanic Technol.*, 4(2), 336–339.
- McComiskey, A., and G. Feingold (2012), The scale problem in quantifying aerosol indirect effects, *Atmos. Chem. Phys.*, 12(2), 1031–1049.
- Pekour, M. S., B. Schmid, D. Chand, J. M. Hubbe, C. D. Kluzek, D. A. Nelson, J. M. Tomlinson, and D. J. Cziczo (2013), Development of a new airborne humidigraph system, *Aerosol Sci. Technol.*, 47(2), 201–207, doi:10.1080/02786826.2012.741274.
- Pilewskie, P., M. Rabbette, R. Bergstrom, J. Marquez, B. Schmid, and P. B. Russell (2000), The discrepancy between measured and modeled downwelling solar irradiance at the ground: Dependence on water vapor, *Geophys. Res. Lett.*, 27(1), 137–140, doi:10.1029/1999GL011085.
- Pitts, M. C., L. W. Thomason, J. M. Zawodny, B. N. Wenny, J. M. Livingston, P. B. Russell, J. H. Yee, W. H. Swartz, and R. E. Shetter (2006), Ozone observations by the gas and aerosol measurement sensor during SOLVE II, *Atmos. Chem. Phys.*, 6(9), 2695–2709, doi:10.5194/acp-6-2695-2006.
- Redemann, J., S. J. Masonis, B. Schmid, T. L. Anderson, P. B. Russell, J. M. Livingston, O. Dubovik, and A. D. Clarke (2003), Clear-column closure studies of aerosols and water vapor aboard the NCAR C-130 during ACE-Asia, 2001, *J. Geophys. Res.*, 108(D23), 8655, doi:10.1029/2003JD003442.
- Redemann, J., B. Schmid, J. A. Eilers, R. Kahn, R. C. Levy, P. B. Russell, J. M. Livingston, P. V. Hobbs, W. L. Smith, and B. N. Holben (2005), Suborbital measurements of spectral aerosol optical depth and its variability at subsatellite grid scales in support of CLAMS 2001, *J. Atmos. Sci.*, 62(4), 993–1007.
- Redemann, J., Q. Zhang, P. B. Russell, J. M. Livingston, and L. A. Remer (2009), Case studies of aerosol remote sensing in the vicinity of clouds, *J. Geophys. Res.*, 114, D06209, doi:10.1029/2008JD010774.
- Revercomb, H. E., et al. (2003), The ARM Program's water vapor intensive observation periods, *Bull. Am. Meteorol. Soc.*, 84(2), 217–236, doi:10.1175/BAMS-84-2-217.
- Richard, C., et al. (2012), New section of the HITRAN database: Collision-induced absorption (CIA), *J. Quant. Spectrosc. Radiat. Transfer*, 113(11), 1276–1285, doi:10.1016/j.jqsrt.2011.11.004.
- Rogers, R. R., et al. (2009), NASA LaRC airborne high spectral resolution lidar aerosol measurements during MILAGRO: Observations and validation, *Atmos. Chem. Phys.*, 9(14), 4811–4826.
- Russell, P. B., T. Matsumoto, V. J. Banta, J. M. Livingston, C. Mina, D. S. Colburn, and R. F. Pueschel (1986), Measurements with an airborne, autotracking, external-head sunphotometer, Preprint Volume, Sixth Conference on Atmospheric Radiation, May 13–16, 1986, Amer. Meteor. Soc., Boston, MA, 55–58.
- Russell, P. B., et al. (1993a), Pinatubo and pre-Pinatubo optical-depth spectra: Mauna Loa measurements, comparisons, inferred particle size distributions, radiative effects, and relationship to lidar data, *J. Geophys. Res.*, 98(D12), 22,969–22,985.
- Russell, P. B., et al. (1993b), Post-Pinatubo optical depth spectra vs. latitude and vortex structure: Airborne tracking sunphotometer measurements in AASe II, *Geophys. Res. Lett.*, 20(22), 2571–2574.
- Russell, P. B., J. M. Livingston, P. Hignett, S. Kinne, J. Wong, A. Chien, R. Bergstrom, P. Durkee, and P. V. Hobbs (1999), Aerosol-induced radiative flux changes off the United States mid-Atlantic coast: Comparison of values calculated from sunphotometer and in situ data with those measured by airborne pyranometer, *J. Geophys. Res.*, 104(D2), 2289–2307.
- Russell, P. B., J. M. Livingston, O. Dubovik, S. A. Ramirez, J. Wang, J. Redemann, B. Schmid, M. Box, and B. N. Holben (2004), Sunlight transmission through desert dust and marine aerosols: Diffuse light corrections to Sun photometry and pyrheliometry, *J. Geophys. Res.*, 109, D08207, doi:10.1029/2003JD004292.
- Russell, P. B., et al. (2007), Multi-grid-cell validation of satellite aerosol property retrievals in INTEx/ITCT/ICARTT 2004, *J. Geophys. Res.*, 112, D12S09, doi:10.1029/2006JD007606.
- Schmid, B., and C. Wehrli (1995), Comparison of Sun photometer calibration by use of the Langley technique and the standard lamp, *Appl. Opt.*, 34(21), 4500–4512.
- Schmid, B., K. J. Thorne, P. Demoulin, R. Peter, C. Mätzler, and J. Sekler (1996), Comparison of modeled and empirical approaches for retrieving columnar water vapor from solar transmittance measurements in the 0.94- $\mu$ m region, *J. Geophys. Res.*, 101(D5), 9345–9358, doi:10.1029/96JD00337.
- Schmid, B., P. R. Spyak, S. F. Biggar, C. Wehrli, J. Sekler, T. Ingold, C. Mätzler, and N. Kämpfer (1998), Evaluation of the applicability of solar and lamp radiometric calibrations of a precision Sun photometer operating between 300 and 1025 nm, *Appl. Opt.*, 37, 3923–3941.
- Schmid, B., et al. (2000), Clear-sky closure studies of lower tropospheric aerosol and water vapor during ACE-2 using airborne sunphotometer, airborne in-situ, space-borne, and ground-based measurements, *Tellus B*, 52(2), 568–593, doi:10.1034/j.1600-0889.2000.00009.x.
- Schmid, B., et al. (2001), Comparison of columnar water-vapor measurements from solar transmittance methods, *Appl. Opt.*, 40(12), 1886–1896.
- Schmid, B., et al. (2003a), Column closure studies of lower tropospheric aerosol and water vapor during ACE-Asia using airborne Sun photometer and airborne in situ and ship-based lidar measurements, *J. Geophys. Res.*, 108(D23), 8656, doi:10.1029/2002JD003361.
- Schmid, B., et al. (2003b), Coordinated airborne, spaceborne, and ground-based measurements of massive thick aerosol layers during the dry season in southern Africa, *J. Geophys. Res.*, 108(D13), 8496, doi:10.1029/2002JD002297.
- Schmid, B., et al. (2006), How well do state-of-the-art techniques measuring the vertical profile of tropospheric aerosol extinction compare?, *J. Geophys. Res.*, 111, D05S07, doi:10.1029/2005JD005837.
- Segal-Rosenheimer, M., P. B. Russell, J. M. Livingston, S. Ramachandran, J. Redemann, and B. A. Baum (2013a), Retrieval of cirrus properties by Sun photometry: A new perspective on an old issue, *J. Geophys. Res. Atmos.*, 118, 4503–4520, doi:10.1002/jgrd.50185.
- Segal-Rosenheimer, M., et al. (2013b), Tracking elevated pollution layers with a newly developed hyperspectral Sun/sky spectrometer (4STAR): Results from the TCAP 2012 and 2013 campaigns, *JGR*, in review.
- Shinozuka, Y., and J. Redemann (2011), Horizontal variability of aerosol optical depth observed during the ARCTAS airborne experiment, *Atmos. Chem. Phys.*, 11(16), 8489–8495.

- Shinozuka, Y., A. D. Clarke, S. G. Howell, V. N. Kapustin, C. S. McNaughton, J. Zhou, and B. E. Anderson (2007), Aircraft profiles of aerosol microphysics and optical properties over North America: Aerosol optical depth and its association with PM<sub>2.5</sub> and water uptake, *J. Geophys. Res.*, *112*(D12), doi:10.1029/2006JD007918.
- Shinozuka, Y., et al. (2011), Airborne observation of aerosol optical depth during ARCTAS: Vertical profiles, inter-comparison and fine-mode fraction, *Atmos. Chem. Phys.*, *11*(8), 3673–3688.
- Sinyuk, A., B. N. Holben, A. Smirnov, T. F. Eck, I. Slutsker, J. S. Schafer, D. M. Giles, and M. Sorokin (2012), Assessment of error in aerosol optical depth measured by AERONET due to aerosol forward scattering, *Geophys. Res. Lett.*, *39*, L23806, doi:10.1029/2012GL053894.
- Smirnov, A., B. N. Holben, T. F. Eck, O. Dubovik, and I. Slutsker (2000), Cloud screening and quality control algorithms for the AERONET database, *Remote Sens. Environ.*, *73*, 337–349.
- Swartz, W. H., J. H. Yee, R. E. Shetter, S. R. Hall, B. L. Lefer, J. M. Livingston, P. B. Russell, E. V. Browell, and M. A. Avery (2005), Column ozone and aerosol optical properties retrieved from direct solar irradiance measurements during SOLVE II, *Atmos. Chem. Phys.*, *5*(3), 611–622, doi:10.5194/acp-5-611-2005.
- Vandaele, A. C., C. Hermans, P. C. Simon, M. Carleer, R. Colin, S. Fally, M. F. Mérienne, A. Jenouvrier, and B. Coquart (1998), Measurements of the NO<sub>2</sub> absorption cross-section from 42 000 cm<sup>−1</sup> to 10 000 cm<sup>−1</sup> (238–1000 nm) at 220 K and 294 K, *J. Quant. Spectros. Radiat. Transfer*, *59*(3–5), 171–184, doi:10.1016/S0022-4073(97)00168-4.
- Zieger, P., T. Ruhtz, R. Preusker, and J. Fischer (2007), Dual-aureole and sun spectrometer system for airborne measurements of aerosol optical properties, *Appl. Opt.*, *46*(35), 8542–8552, doi:10.1364/AO.46.008542.
- Ziemba, L. D., et al. (2013), Airborne observations of aerosol extinction by in-situ and remote-sensing techniques: Evaluation of particle hygroscopicity, *Geophys. Res. Lett.*, *40*, 417–422, doi:10.1029/2012GL054428.